Inorganic Chemistry

Article

pubs.acs.org/IC

Synthesis, Crystal Structure, and Proton Conductivity of One-Dimensional, Two-Dimensional, and Three-Dimensional Zirconium Phosphonates Based on Glyphosate and Glyphosine

Marco Taddei,* Anna Donnadio,* Ferdinando Costantino, Riccardo Vivani, and Mario Casciola

Dipartimento di Chimica, Università di Perugia, Via Elce di Sotto 8, 06123 Perugia, Italy

Supporting Information

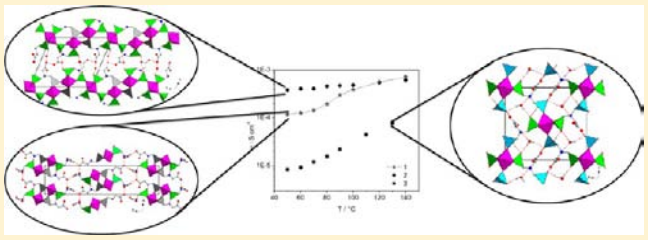

ABSTRACT: The reaction of two small phosphono-amino acids based on glycine (glyphosine and glyphosate) with zirconium under mild conditions led to the attainment of three related zirconium derivatives with 1D, 2D, and 3D structures of formulas $ZrF[H_3(O_3PCH_2NHCH_2COO)_2]$ (**1**), $Zr_3H_8[(O_3PCH_2)_2NCH_2COO]_4\cdot 2H_2O$ (**2**), and $Zr[(O_3PCH_2)(HO_3PCH_2)NHCH_2COOH]_2\cdot 2H_2O$ (**3**), respectively, whose structures were solved by X-ray powder and single-crystal diffraction data. The glyphosate derivative has 1D ribbon-type structure whereas the dimensionality of the glyphosine-derived materials (2D and 3D) can be tuned by changing the synthesis conditions. The low-dimensional compounds (**1** and **2**) can be directly produced in the form of nanoparticles with different size and morphology whereas the 3D compound (**3**) has a higher crystallinity and can be obtained as single crystals with a prismatic shape. The different structural dimensionality reflects the shape and size of the crystals and also differently affects the proton conductivity properties, measured over a wide range of temperature at 95% relative humidity. Their high thermal and chemical stability together with the small size may promote their use as fillers for polymeric electrolyte membranes for fuel cells applications.

INTRODUCTION

The chemistry of zirconium phosphonates, widely developed at the beginning of the 1970s, has enjoyed a resurgence in recent years.[1] Many derivatives have been built by using aminomethylenephosphonic acids that are building blocks with a higher structural versatility, if compared to other organophosphonates with a linear structure, which give rise to zirconium derivative compounds based on α-type layers.[2] The use of such aminomethylenephosphonates has allowed us to obtain new compounds with structures ranging from 1D to 2D to 3D. Among them, a number of new archetypes have been recently discovered.[3]

The access to a wide range of structural arrangements, together with the possibility of using building blocks with various functional groups, may represent a powerful tool in the design of materials for specific applications, such as heterogeneous catalysts, ion exchangers, fillers for composite membranes, solid-state proton conductors, and many others.[4]

The latter above-mentioned property is currently of great interest: the progressive availability of solid proton-conducting materials stimulated the utilization of proton conduction in a variety of devices, including fuel cells, electrolyzers, chemical sensors, electrochromic displays, and hydrogen pumps.[5] Proton-conducting polymers and ceramic oxides are widely investigated as solid electrolytes in fuel cell working at low (60−80 °C) or high (>700 °C) temperature, respectively.[6] Nanosized proton conductors are also employed as fillers for proton-conducting polymers in order to improve their electrical conductivity and mechanical properties while reducing the membrane permeability to oxygen and fuel.[7] As a consequence, there is a growing demand for new solid-state proton conductors with good conductivity performance under different conditions of humidity and temperature.

Hybrid inorganic−organic materials, built from the rational assembly of metal ions and various organic ligands bearing acidic groups, have shown promising perspectives in this field. As a matter of fact, in the last few years the number of papers reporting the conductivity properties of hybrid coordination polymers and metal organic framework (MOF) materials have grown exponentially.[8] Most of them are conventional carboxylate-based MOFs modified with free strong acids[9] and/or heterocyclic moieties.[10]

Some of these materials showed high anhydrous conductivity at different temperatures. However, the best-performing materials are affected by several limitations such as scarce chemical and thermal stability, the reproducibility of the conductivity values after many cycles, the volatility of the acidic guest molecules responsible for the high conductivity values, and the scarce compatibility of these compounds to be dispersed in conductive polymeric matrices for a real employment in fuel cell application.

The search for new conductive materials should instead include the following features: low dimensionality and

Received: July 29, 2013
Published: September 27, 2013

ACS Publications © 2013 American Chemical Society

nanometric dimensions to improving the degree of dispersion in polymeric matrices, good thermal and chemical stability, and the acidic groups covalently linked to the inorganic substrate to enhance the stability under various conditions. Among others, in the past zirconium phosphates and phosphonates have been shown to possess many of the above cited characteristics, together with interesting properties as solid-state proton conductors working in relatively low temperature ranges. In fact, they couple good conductivity properties with excellent thermal and chemical stability and very low solubility, allowing their use under almost all of the experimental conditions required for this specific application.

To date, the highest conductivity was reported for zirconium *m*-sulfophenylphosphonate-methylphosphonate, a compound with formula $Zr(O_3PCH_3)_{0.65}(O_3PC_6H_4SO_3H)_{1.3}$, reaching values on the order of 10^{-1} S cm^{-1}, measured at 90% relative humidity. The main drawback of this compound is its scarce stability under very humid conditions because in the presence of water it undergoes bonds cleavage between the PO_3 group and Zr atom, thus losing the superacidic sulfophenyl moiety, which is responsible for the excellent conductivity.[11]

Among zirconium aminomethylenephosphonates, the proton conductivity of a 3D compound has solely been investigated to date. This compound was able to reach values on the order of 10^{-4} S cm^{-1}, which decreased after a phase transition that caused the rearrangement of the water molecules contained inside the channels present in its structure.[12]

In this Article, we report on the synthesis, structure, and results of conductivity measurements of three zirconium aminomethylenephosphonates based on two building blocks derived from glycine: glyphosate, a monophosphonic acid, and glyphosine, a diphosphonic acid (Chart 1).

Chart 1. Molecular Structure of the Two Ligands Used

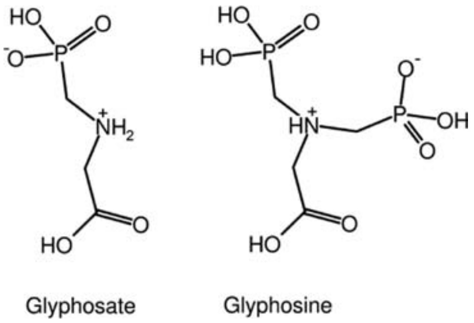

In the literature, some reports can be found where the use of zirconium derivatives of the same building blocks for various purposes is reported, but the structures were not solved and attributed to the conventional α-type.[13] The structures of two of our compounds were solved ab initio from PXRD data, and the other was solved from single-crystal data: all of these compounds show structural arrangements that are unprecedented in zirconium phosphonate chemistry. The compounds were characterized by conductivity measurements as a function of temperature at 95% relative humidity.

■ EXPERIMENTAL SECTION

Chemicals. $ZrOCl_2 \cdot 8H_2O$ was a Merck Pro Analysi product. All of the other chemicals were purchased from Sigma-Aldrich. All reagents were used as received without further purification.

Synthesis of $ZrF[H_3(O_3PCH_2NHCH_2COO)_2]$ (1). **1** was prepared as follows: a clear solution of glyphosate (338 mg, 2 mmol) in 20 mL of water was added to a solution of $ZrOCl_2 \cdot 8H_2O$ (322 mg, 1 mmol) in 2.9 M HF (1.4 mL, 4 mmol). The starting pH was 2.17. This mixture was maintained in a closed plastic vessel at 80 °C for 2 days. The white precipitate was filtered under vacuum, washed with water, and dried at 80 °C. A 300 mg quantity of product was recovered. Yield = 68% (calculated on the basis of Zr).

Analysis Calcd for $C_6H_{13}N_2O_{10}FP_2Zr$ (**1**): C = 16.2%, H = 2.9%, N = 6.3%, P = 13.9%, Zr = 20.5%. Found: C = 16.6%, H = 2.2%, N = 5.4%, P = 14.3%, Zr = 20.8%.

Synthesis of $Zr_3H_8[(O_3PCH_2)_2NCH_2COO]_4 \cdot 2H_2O$ (2). **2** was prepared as follows: a clear solution of glyphosine (2.62 g, 10 mmol) in 75 mL of water was added to a solution of $ZrOCl_2 \cdot 8H_2O$ (1.61 g, 5 mmol) in 2.9 M HF (15.5 mL, 45 mmol). The starting pH was 2.10. This mixture was maintained in a closed plastic vessel at 80 °C for 4days. The white precipitate was centrifuged, washed with water,and dried at 60 °C. A 1.22 g quantity of product was recovered. Yield = 54% (calculated on the basis of Zr).

Analysis Calcd for $C_{16}H_{36}N_4O_{34}P_8Zr_3$ (**2**): C = 13.3%, H = 2.8%, N = 3.9%, P = 17.2%, Zr = 20.2%. Found: C = 12.4%, H = 2.9%, N = 3.9%, P = 17.7%, Zr = 20.0%.

Synthesis of $Zr[(O_3PCH_2)(HO_3PCH_2)NHCH_2COOH]_2 \cdot 2H_2O$ (3). **3** was prepared as follows: a clear solution of glyphosine (524 mg, 2 mmol) in 15 mL of water was added to a solution of $ZrOCl_2 \cdot 8H_2O$ (322 mg, 1 mmol) in 2.9 M HF (4.1 mL, 12 mmol). The starting pH was 2.18. This mixture was maintained in a closed plastic vessel at 80 °C for 7 days. The white single crystals were separated by filtration under vacuum and washed with water. A 220 mg quantity of product was recovered. Yield = 35% (calculated on the basis of Zr).

Analysis Calcd for $C_8H_{22}N_2O_{18}P_4Zr$ (**3**): C = 14.8%, H = 3.4%, N = 4.3%, P = 19.1%, Zr = 14.0%. Found: C = 15.4%, H = 2.9%, N = 4.8%, P = 18.2%, Zr = 14.3%.

The phase purity of polycrystalline samples used herein was checked by a comparison of the experimental PXRD with that calculated from the crystal structure.

Analytical Procedures. Zirconium and phosphorus contents of samples were obtained by inductively coupled plasma−optical emission spectrophotometry (ICP−OES) using a Varian Liberty Series II instrument working in axial geometry after the mineralization of samples with hydrofluoric acid.

Carbon, nitrogen, and hydrogen contents were determined by elemental analysis using an EA 1108 CHN Fisons instrument.

PXRD patterns for structure determination and Rietveld refinements were collected with Cu Kα radiation on a PANalytical X'PERT PRO diffractometer, PW3050 goniometer equipped with an X'Celerator detector. The long fine focus (LFF) ceramic tube operated at 40 kV and 40 mA. To minimize preferential orientations of the microcrystals, the samples were carefully side-loaded onto an aluminum sample holder with an oriented quartz monocrystal underneath.

Thermogravimetric (TG) measurements were performed using a Netzsch STA490C thermoanalyser under a 20 mL min^{-1} air flux with a heating rate of 5 °C min^{-1}.

FE-SEM images were collected with an LEO 1525 ZEISS instrument working with an acceleration voltage of 15 kV.

Conductivity measurements were carried out on pellets of pressed powder by impedance spectroscopy with a Solartron Sl 1260 impedance/gain phase analyzer in the frequency range of 10 Hz−1 MHz at a signal amplitude of ≤100 mV. Pellets, 10 mm in diameter and 1−1.5 mm thick, were prepared by pressing ~200 mg of material at 40 kN/cm^2. The two flat surfaces of the pellet were coated with a thin layer of pressed platinum black (Aldrich) mixed with the powder in a 3:1 ratio. The impedance data were fitted to a suitable equivalent circuit by Zview 2 software (Scribner Associates, Inc.). Details on the complex impedance equation used for curve fitting are reported in the Supporting Information. The pellet conductivity was determined at increasing temperature between 50 and 140 °C at 95% relative humidity (RH). The RH was controlled as described previously.[14] All of the conductivity values here reported refer to measurements carried

Table 1. Structural Data and Refinement Details for **1**−**3**

compound	**1**	**2**	**3**
empirical formula	$C_6H_{13}N_2O_{10}FP_2Zr$	$C_{16}H_{36}N_4O_{34}P_8Zr_3$	$C_8H_{22}N_2O_{18}P_4Zr$
formula weight	445.24	1349.62	649.38
crystal system	monoclinic	triclinic	monoclinic
space group	$P2_1/n$	P-1	$P2_1/n$
a/Å	8.5729(3)	5.3770(2)	5.4563(6)
b/Å	32.764(1)	13.3379(7)	14.934(1)
c/Å	5.3041(1)	15.5360(5)	13.282(1)
α/deg		111.959(3)	
β/deg	105.693(3)	96.402(5)	95.525(8)
γ/deg		94.863(3)	
volume/Å^3	1434.28(8)	1017.21(5)	1077.3(2)
Z	4	1	2
calculated density/g·cm^{-3}	2.06	2.20	2.00
μ/mm^{-1}			0.899
$F(000)$			672
data range/2θ·deg^{-1}	3−120	5−120	3.13−28.56
wavelength	1.54056	1.54056	0.71069
No. of data points	7001	6765	2566
reflections collected, unique	2112	2996	7453, 2566
R_{int}			0.0323
No. of parameters	98	121	166
No. of restraints	59	100	6
R_p	0.0344	0.0302	
R_{wp}	0.0454	0.0397	
R_F2	0.0469	0.0351	
R_1, $_wR_2$ [$I > 2\sigma(I)$]			0.0330, 0.1196
R_1, $_wR_2$ (all data)			0.0537, 0.1263
largest diff. peak and hole/eÅ^{-3}			+0.410, −0.518
GOF	2.89	2.55	1.076

out after the conductivity had reached a constant value for at least 2 hours. Water uptake at controlled temperature and RH was determined by means of a cell having the same size and shape as the conductivity cell and differing from that mainly because the pellet holder is replaced by a glass container hosting the sample.[14] The cell is equipped with a device that allows the closure of the sample container with a Teflon plug without opening the cell. After a suitable equilibration time (usually 1 day) at the desired temperature and RH, the sample container is closed, extracted from the cell, and weighed. The water content is determined on the basis of the weight of the sample dried at 120 °C by taking into account the amount of water trapped in the sample container at the temperature and RH of the experiment.

Structure Determination and Refinement for 1−3. The crystal structures of **1** and **2** were solved ab initio from PXRD data. Indexing was performed using both the TREOR and the DICVOL06 programs.[15] Space groups were assigned using the Chekcell program.[16] Structural models were determined using the real space global optimization methods implemented in the FOX program.[17] Trial structures were generated using the parallel tempering algorithm. Rietveld refinements of the structural models were performed using the GSAS program.[18]

The crystal structure of **3** was solved ab initio from single-crystal X-ray data with the direct methods implemented in the SIR97 program[19] and was refined with the SHELX program.[20]

Crystal data and details of the refinement for **1**−**3** are reported in Table 1. Figure 1 shows the final Rietveld and difference plots for **1** and **2**.

■ RESULTS AND DISCUSSION

Description of the Structures. **1** has a 1D structure consisting of the packing of hybrid inorganic chains running

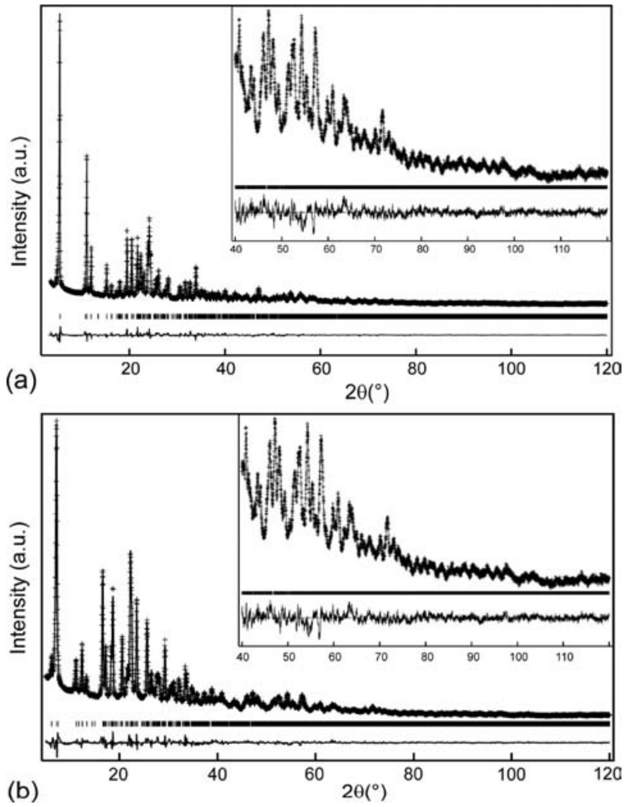

Figure 1. Final Rietveld and difference plots for (a) **1** and (b) **2**.

along the *c* axis and arranged in a herringbone fashion (Figure 2).

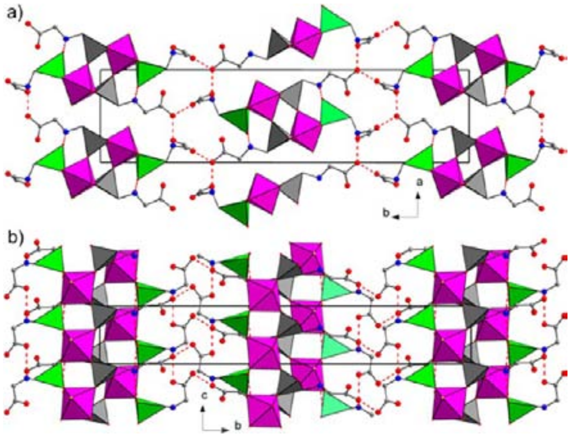

Figure 2. Polyhedral structure of **1** viewed along (a) the *c* axis and (b) the *a* axis. ZrO_5F octahedra are represented in purple, bidentate PO_3C tetrahedra are represented in green, and tridentate PO_3C tetrahedra are represented in gray. Hydrogen bonds are represented as red dashed lines.

These chains are made of connected zirconium octahedra and phosphorus tetrahedra. The zirconium atoms are coordinated by a fluorine atom and by five oxygen atoms belonging to five different phosphonate tetrahedra in the remaining positions. The two phosphonate groups are not equivalent: one is tridentate, coordinating three different metal atoms, and the other is bidentate, coordinating two different metal atoms and with the free oxygen pointing toward the crystallographically equivalent nitrogen atoms (N5) of two adjacent tridentate ligands, forming two hydrogen bonds (P−O···N distances = 2.79(2) Å, 3.03(2) Å). The chains are originated by the connection of two arrays of zirconium atoms via the tridentate phosphonate groups, which connect two metal atoms of the same array along the *c* axis and one atom of the second array. The organic moieties are pending from the inorganic framework, occupying the region among the chains; the carboxylic groups are involved in hydrogen bonds with both analogous groups from the nearest chains along the *b* axis (O1···O11 distance = 2.45(2) Å) and with N15 (O12···N15 distance = 2.90(2) Å, O1···N15 distance = 2.66(2) Å). The presence of $-NH_2^+$ groups (as shown by the bands in the 2300−2900 cm^{-1} region of the IR spectrum, available as Supporting Information) allows the establishment of a large number of hydrogen bonds in such a way that the structure is connected in three dimensions by these noncovalent interactions.

2 has a layered structure based on the connection of two different kinds of monodimensional chains of ZrO_6 octahedra and PO_3C tetrahedra, both running along the *a* axis and connected via phosphonate tetrahedra along the *c* axis (Figures 3 and 4).

One of these chains (A type) is built from the connectivity along the *a* axis of two symmetry-related Zr1 octahedra via the tridentate (connecting three different metal atoms) P8 tetrahedra and the bidentate (connecting two different metal atoms) P16 tetrahedra; this arrangement is similar to that found in compound **1**. The difference is that in this case, in place of the fluorine atom found in **1**, there is an oxygen atom belonging to the bidentate P23 tetrahedra that connect one Zr1 belonging to an A-type chain to the Zr2 of a B-type chain: this kind of chain consists of Zr2 octahedra, placed in a special position with multiplicity 1, connected along the *a* axis by the bidentate (connecting two different metal atoms) P1 tetrahedra. Every zirconium atom of the B-type chain, residing in an inversion center, is surrounded by four P1 tetrahedra and two P23 tetrahedra. The P/Zr ratio in this compound is $^8/_3$, a noninteger value that was never observed before in any zirconium phosphonate. The interlayer distance is 13.3 Å, and the interlayer space is occupied by the organic pendant groups and one water molecule per formula unit. There is a network of hydrogen bonds involving the carboxylate groups, the intercalated water molecules, and the free P−O groups. The nitrogen atoms are protonated, but they do not seem to be involved in any hydrogen bonding interaction.

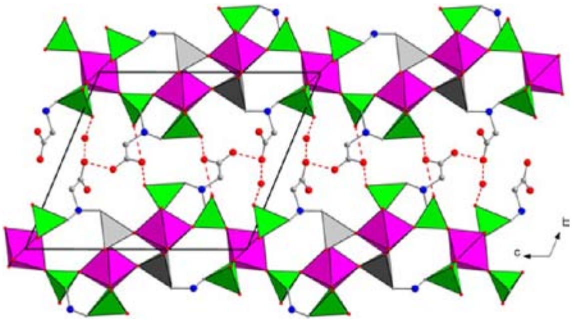

Figure 3. Polyhedral structure of **2** viewed along the *a* axis. ZrO_6 octahedra are represented in purple, bidentate PO_3C tetrahedra are represented in green, and tridentate PO_3C tetrahedra are represented in gray. Hydrogen bonds are represented as red dashed lines.

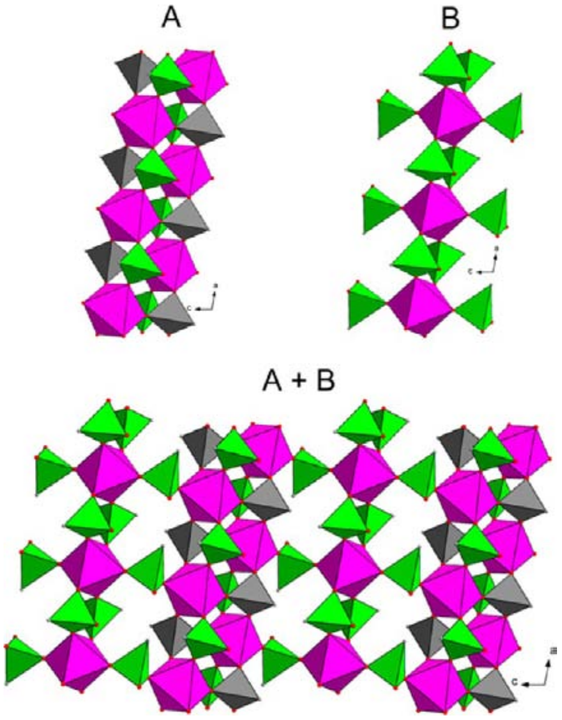

Figure 4. Building of one inorganic layer of **2** from the connection of A- and B-type chains. ZrO_6 octahedra are represented in purple, bidentate PO_3C tetrahedra are represented in green, and tridentate PO_3C tetrahedra are represented in gray.

3 has a 3D structure based on monodimensional inorganic chains composed of ZrO_6 octahedra and PO_3C tetrahedra, running along the *a* axis and connected by the glyphosine moieties in the other dimensions. Every zirconium atom lies on an inversion center and is surrounded by four bidentate phosphonate groups and two monodentate phosphonate groups so that opposite phosphonate groups coordinated to it are crystallographically equivalent (Figure 5).

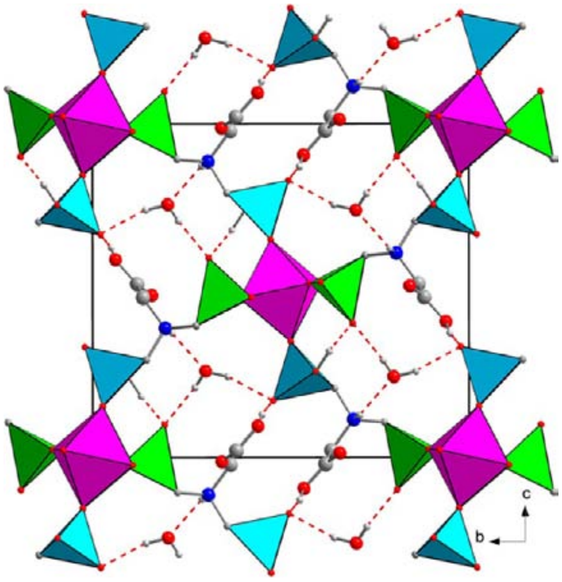

Figure 5. Polyhedral structure of **3** viewed along the *a* axis. ZrO_6 octahedra are represented in purple, bidentate PO_3C tetrahedra are represented in green, and monodentate PO_3C tetrahedra are represented in light blue. Hydrogen bonds are represented as red dashed lines.

Every chain is connected to four other chains via the organic ligands, with each of them bearing one monodentate and one bidentate PO_3C tetrahedra. The monodentate tetrahedron has one free P−OH and one free P═O group, and the bidentate tetrahedron has a free P−O group: each of these groups is involved in a network of hydrogen bonds with the carboxylic group, the protonated nitrogen atom, and the water molecule residing in the small channels present in the structure. Every channel originates from the subdivision in 2 equal parts of a 32-membered ring window, as shown in Figure 6.

Thermal Behavior. Figure 7 shows the TG curves for **1**−**3**.

1 is stable up to 300 °C, when the organic part of the framework starts decomposing, until only ZrP_2O_7 is left at 1200 °C. The observed weight loss is 39.9%, in good agreement with the calculated value (40.5%).

2 shows an initial weight loss at around 100 °C resulting from the loss of two water molecules per formula unit (observed, 3.2%; calculated, 2.7%). The second step of weight loss, occurring between 200 and 400 °C, is due to the decarboxylation of the glycine moieties: four CO_2 molecules per formula unit are lost, corresponding to a calculated loss of 13.0%, which is well matched by the 13.8% observed value. The compound continues to lose weight after 400 °C, but the following steps are not resolved. The total weight loss at 1200 °C is 32.4%.

3 shows the first weight loss occurring around 200 °C resulting from the loss of the water molecules held inside the channels present in its structure. The observed loss is 5.2%, in good agreement with the calculated loss (5.5%). The other weight loss steps are not resolved, and the final weight loss is 49.8%.

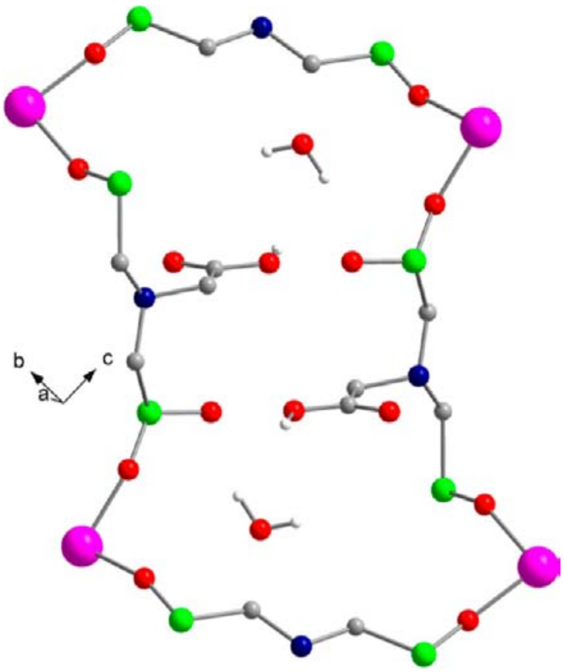

Figure 6. Structure of the 32-membered ring showing the position of water molecules in **3**.

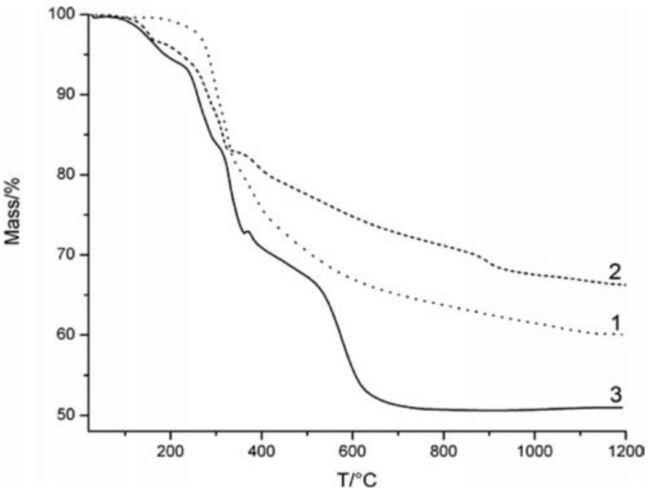

Figure 7. TG curves for **1** (dotted), **2** (dashed), and **3** (solid).

Morphological and Microstructural Characterization. FE-SEM images (Figure 8a,b) revealed that **1** and **2** have nanometric dimensions whereas **3** consists of well-shaped submillimetric prismatic crystals (Figure 8c and its inset). **1** is composed of ribbon-type nanocrystals with a high aspect ratio of the particles. Figure 8a shows a population of rod-shaped nanocrystals with a cross section as small as 100 to 200 nm and different lengths in the 200 nm−1 μm range. **2** consists of platelet rectangular particles with a homogeneous size and a lateral section of about 200 nm. The length is in the 800 nm to 2 μm range (Figure 8b). Although it is difficult to get good images at higher magnification, these particles look to be quite thin as the thickness in the third dimension can be estimated to be about 50 to 80 nm (inset of Figure 8b).

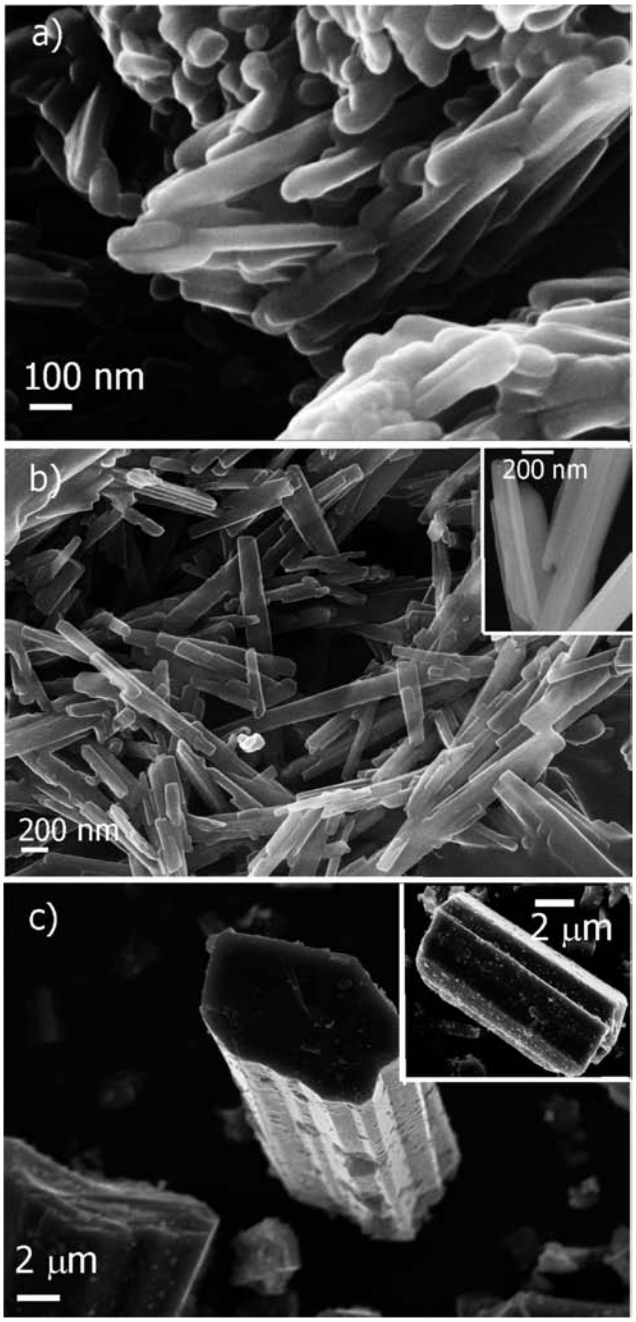

Figure 8. FE-SEM images of (a) **1**, (b) **2**, and (c) **3**.

The morphological features of **1** and **2** enlightened by SEM analysis can be correlated with their crystallographic structure by means of a microstructural investigation performed with the Rietveld method, using the GSAS-EXPGUI software package, following the method described in a previous publication.[21]

Generally speaking, the morphological anisotropy typical of low-dimensional compounds is reflected in the XRD pattern as anisotropically broadened peaks because the thickness of crystallite under the scattering plane is one of the main factors affecting the broadening of peaks. Lattice defects, or microstrain, can also affect diffraction peak broadening, especially in nanocrystals, where the interplanar distances can change between the core and the surface of the particles and when the structure is highly defective. However, strain- and size-related contributions are different functions of the diffraction angle, so they can be evaluated separately.[22]

A third microstructural factor that may contribute to the whole broadening of Bragg peaks is the presence of stacking faults in the crystals. The modification of the diffraction peak profiles associated with the family of planes that contain these faults is similar to that caused by a size effect,[23] and the discrimination of these two contributions is not trivial: in this work, we have neglected stacking fault effects. This approximation may overestimate the size-related contribution; therefore, we may consider that the obtained size values are minimum sizes.

The diffraction profiles were modeled by a pseudo-Voigt function (profile function no. 3 in GSAS).[18,23] The peak broadening was modeled by employing *Xe* and *Ye* anisotropic contributions to the peak-shape function, along the [010] anisotropic broadening axis for both samples. The instrumental contribution to the peak broadening was previously evaluated by the Rietveld refinement of the profile of lanthanum hexaboride, LaB_6, as an external peak profile standard. We assumed that the standard was not affected by microstrain, and the instrumental broadening was modeled by the refinement of *W* and *Y* peak shape parameters for Gaussian and Lorentzian contributions, respectively. For samples 1 and 2, the refined peak shape parameters were *P*, *X*, and *Xe*, accounting for Gaussian and Lorentzian contributions to size effects, and *U*, *Y*, and *Ye* for the corresponding microstrain effects, whereas *W* was fixed at the value refined on the standard. Two additional parameters for modeling asymmetry at low angle were also refined.

The coherent domain sizes (volume-weighted) parallel and perpendicular to the broadening axis were estimated using the equations

$$Dv_{\parallel} = \frac{1800\lambda}{\pi(X + Xe)}$$

and

$$Dv_{\perp} = \frac{1800\lambda}{\pi X}$$

respectively and the corresponding microstrain values were calculated with the following equations

$$\varepsilon_{\parallel} = \left(\frac{\pi}{18\,000}\right)(Y + Ye - Yi)$$

and

$$\varepsilon_{\parallel} = \left(\frac{p}{18\,000}\right)(Y - Yi)$$

in which *Yi* is the instrumental contribution obtained by the refinement of the LaB_6 pattern.[24]

The results of this analysis are reported in Table 2.

For both samples, the differences between coherent domain sizes are not as marked as the large form factor shown by SEM

Table 2. Microstructural Parameters for 1 and 2

sample	1	2
$Dv_{\parallel}$ (nm)	270	65
$Dv_{\perp}$ (nm)	135	130
$\varepsilon_{\parallel} \times 10^3$	3	
$\varepsilon_{\perp} \times 10^3$	3	

analysis may suggest. For **1**, the preferred elongation direction corresponds to the *b* axis, that is, along one direction of chain packing. We may therefore assume that microcrystals are also elongated along this direction. For **2**, the crystalline domains are larger along the *ac* plane, that is, the plane of layers. Also in this case it is likely that the preferred growth direction of microcrystals lies along this plane. However, in both samples, the larger coherent domain sizes are smaller than the average length of microcrystals observed by SEM. This discrepancy may be explained by assuming a certain mosaicity of crystals.

Microstrain is very low and does not show relevant anisotropy.

Proton Conductivity. The complex impedance ($Z^* = Z' + iZ''$) of pellets made of **1**−**3** was measured as a function of temperature at 95% relative humidity (RH). All of the Nyquist plots (Z'' vs Z') show a circular arc appearing at the highest frequencies, well separated from a linear low-frequency tail. These features of the Nyquist plots are usually associated with the series-combination of the pellet impedance (arc) with that of the electrode−pellet interface (tail). As an example, Figure 9 shows the Nyquist plots for sample **3**. Accordingly, with decreasing frequency, the equivalent parallel capacitance associated with the low-frequency tail increases up to 10^{-7}–10^{-5} F at 10 Hz, which are typical values of the electrode−electrolyte interface (Figure S3). In addition, the equivalent parallel capacitance associated with the circular arc is on the order of 10^{-10}–10^{-11} F, thus supporting the assignment of the arc to the frequency response of the pellet material. Therefore, the tail extrapolation to the real axis (or the arc extrapolation to the real axis on the low-frequency side) provides the overall pellet resistance (R). Unfortunately, because of the relatively low upper limit of the available frequency range, in most cases the circular arc is ill-defined on the high-frequency side, and this does not allow us to know whether the frequency response of the pellet gives rise to an additional arc at frequencies higher than 1 MHz. As a consequence, the analysis of the impedance data does not allow us to obtain information about the presence of different types of proton transport (such as bulk and/or surface transport) and their contribution to the overall conductivity. The pellet conductivity (σ) was calculated from R by taking into account the thickness (d) and flat surface area (A) of the pellet: $\sigma = {}^{d}/_{RA}$.

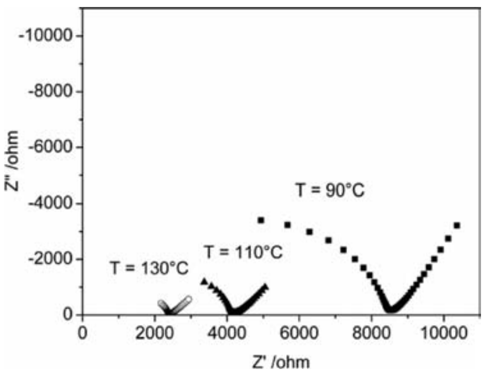

Figure 9. Nyquist plots collected for a pellet of **3** at the indicated temperatures with RH = 95%.

The preparation of the pellet does not affect the structure of the materials (SI), thus indicating that no irreversible transformations take place during the heating run.

The proton conductivity of **1**−**3** as a function of temperature at 95% RH is reported in Figure 10.

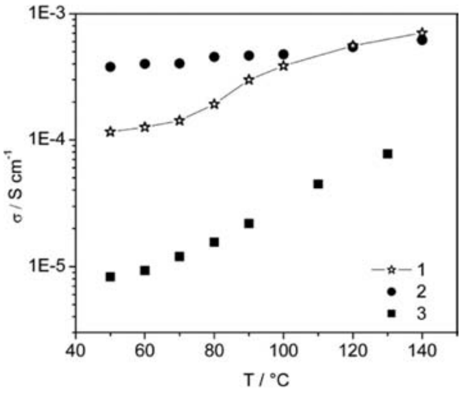

Figure 10. Conductivity as a function of temperature at 95% RH for pellets of **1**−**3**.

Although the conductivity of **2** shows a weak dependence on temperature, the conductivity of pellets of **1** and **3** increases by about 4 and 10 times, respectively, when the temperature increases from 50 to 140 °C. Moreover, the conductivity of **3** is at least 1 order of magnitude lower than the conductivity of **1** within the overall investigated temperature range, probably as a result of the different morphology and crystal size of the **3** particles in comparison with particles of **1** and **2**.

The SEM pictures in Figure 8 show that whereas the samples of **1** and **2** exhibit an elongated morphology with two dimensions in the submicrometer range, the size of the 3D particles is on the order of a few micrometers. A simple calculation based on the average size of the particles allows us to estimate surface-to-volume ratios of around 20, 50, 0.5 μm^{-1} for **1**−**3**, respectively. The much larger surface area per unit volume of the **1** and **2** samples in comparison with **3** may therefore account for their higher proton conductivity.

To gain insight into the different temperature dependence observed for the conductivity of **1** and **2**, water uptake determinations were carried out at 95% RH as a function of temperature. It was found that the hydration of **1** increases from 0 to about 2 water molecules per formula unit in the range of 70−120 °C whereas the hydration of **2** is constant (2 water molecules per formula unit) within the overall temperature range. Therefore the different temperature dependence values of the conductivity of **1** and **2** are concomitant with different changes in their hydration. However, this does not allow us to conclude that the change in the hydration of **1** is fully responsible for the strong increase in its conductivity between 70 and 120 °C because, strictly speaking, the occurrence of reversible structural changes other than hydration changes cannot be excluded. Nevertheless, it seems reasonable to suggest that the increase in hydration makes a non-negligible contribution to the observed conductivity changes of **1**.

The fact that the hydration of **2** is independent of the temperature allowed us to calculate the activation energy of conduction (E_a) on the basis of the Arrhenius equation: $\sigma T = \sigma_0 \exp(-E_a/kT)$, where σ_0 is a pre-exponential factor and k and T are the Boltzmann constant and the absolute temperature, respectively. The E_a value, determined from a least-squares fit of the plot of $\ln(\sigma T)$ versus ${}^{1}/_{T}$, turned out to be 0.1 eV.

The Grotthuss and vehicle mechanisms have been proposed to interpret the proton conduction in solid compounds.

Because the reported activation energies for the Grotthuss and vehicle mechanisms are in the ranges of 0.1−0.4 and 0.5−0.9 eV, respectively, it can be assessed that the conduction mechanism in **2** is of the Grotthuss type.

CONCLUSIONS

Three zirconium phosphonate derivatives of glyphosate and glyphosine were synthesized, and their structures were solved ab initio from powder and single-crystal X-ray diffraction data. These structures were not observed before and confirmed again the high structural versatility of the Zr aminomethylenephosphonate family.

The glyphosine building block was found to form two different nonpolymorphic structures as a function of small changes in the synthesis conditions, in particular, the HF concentration. This behavior is similar to that recently observed for Zr *N*,*N*′-bis(phosphonomethyl)piperazine derivatives, where small changes in the starting pH led to the formation of two phases.[3a]

The different morphology and hydration capabilities of the three compounds were in agreement with their different dimensionality and with the trends observed for their proton conductivity as a function of temperature. In particular, the 1D compound (**1**) can incorporate two water molecules per unit formula, with a consequent increase in the proton conductivity curve that reached values as high as 10^{-3} S cm^{-1} (at 140 °C and 95% RH).

Considering the remarkable proton conductivity, the good thermal and chemical stability, and the small particle sizes of **1** and **2**, we find that they could be excellent fillers for ionomeric membranes for fuel cell applications.

ASSOCIATED CONTENT

Ⓢ Supporting Information

Crystallographic information file, complete crystallographic parameters, and FTIR spectra for **1**−**3**. PXRD spectrum for **3**. PXRD spectra of pellets of **1**−**3** after conductivity measurements.

CCDC 950342−950344 contain crystallographic data for **1**−**3**, respectively. This material is available free of charge via the Internet at http://pubs.acs.org.

AUTHOR INFORMATION

Corresponding Author

*E-mail: marcotaddei@hotmail.com; anna.donnadio@gmail.com.

Notes

The authors declare no competing financial interest.

ACKNOWLEDGMENTS

This work was supported by MIUR - Project FIRB 2010 no. RBFR10CWDA_003.

REFERENCES

(1) (a) Vivani, R.; Alberti, G.; Costantino, F.; Nocchetti, M. *Microporous Mesoporous Mater.* **2008**, *107*, 149−160. (b) Brunet, E.; Alhendawi, H. M. H.; Cerro, C.; de la Mata, M. J.; Juanes, O.; Rodríguez-Ubis, J. C. *Microporous Mesoporous Mater.* **2008**, *138*, 75−85. (c) Clearfield, A. In *Progress in Inorganic Chemistry*; Karlin, K. D., Ed.; John Wiley & Sons: New York, 1998; Vol. *47*, pp 374−510. (d) Vivani, R.; Costantino, F.; Taddei, M. In *Metal Phosphonate Chemistry: From Synthesis to Applications*; Clearfield, A., Demadis, K., Eds.; RSC: Oxford, U.K., 2011; Chapter 2. (e) Brunet, E. In *Metal Phosphonate Chemistry: From Synthesis to Applications*; Clearfield, A., Demadis, K., Eds.; RSC: Oxford, U.K., 2011; Chapter 9.

(2) (a) Clearfield, A.; Costantino, U. In *Comprehensive Supramolecular Chemistry*; Alberti, G., Bein, T., Eds.; Pergamon Press: Oxford, U.K., 1996; Vol. 7, p 107. (b) Alberti, G.; Casciola, M.; Costantino, U.; Vivani, R. *Adv. Mater.* **1996**, *8*, 291−303.

(3) (a) Taddei, M.; Costantino, F.; Vivani, R. *Inorg. Chem.* **2010**, *49*, 9664−9670. (b) Taddei, M.; Costantino, F.; Manuali, V.; Vivani, R. *Inorg. Chem.* **2011**, *50*, 10835−10843. (c) Costantino, F.; Sassi, P.; Geppi, M.; Taddei, M. *Cryst. Growth Des.* **2012**, *12*, 5462−5470. (d) Taddei, M.; Vivani, R.; Costantino, F. *Dalton Trans.* **2013**, *42*, 9671−9678.

(4) (a) Alberti, G.; Casciola, M.; D'Alessandro, E.; Pica, M. *J. Mater. Chem.* **2004**, *14*, 1910−1914. (b) Curini, M.; Rosati, O.; Costantino, U. *Curr. Org. Chem* **2004**, *8*, 591−606. (c) Donnadio, A.; Pica, M.; Taddei, M.; Vivani, R. *J. Mater. Chem.* **2012**, *22*, 5098−5106. (d) Taylor, J. M.; Dawson, K. W.; Shimizu, G. K. H. *J. Am. Chem. Soc.* **2013**, *135*, 1193−1196. (e) Colodrero, R. M. P.; Olivera-Pastor, P.; Losilla, E. R.; Hernandez-Alonso, D.; Aranda, M. A. G.; Leon-Reina; Rius, J.; Moreau, B.; Demadis, K. D.; Villemin, D.; Palomino, M.; Rey, F.; Cabeza, A. *Inorg. Chem.* **2012**, *51*, 7689−7698. (f) Colodrero, R. M. P.; Angeli, G. K; Garcia, M. B.; Olivera-Pastor, P.; Villemin, D.; Losilla, E. R.; Martos, E. Q.; Hix, G. B.; Aranda, M. A. G.; Demadis, K. D.; Cabeza, A. *Inorg. Chem.* **2013**, *52*, 8770−8783.

(5) (a) Alberti, G.; Casciola, M. *Solid State Ionics* **2001**, *145*, 3−16. (b) Kreuer, K. D. *Chem. Mater.* **1996**, *8*, 610−641. (c) Colomban, P., Ed.; *Proton Conductors: Solids, Membranes and Gels Materials and Devices*; Cambridge University Press: Cambridge, U.K., 1992.

(6) (a) Kreuer, K. D. *Solid State Ionics* **1997**, *97*, 1−15. (b) Norby, T. *Solid State Ionics* **1999**, *125*, 1−11.

(7) Alberti, G.; Casciola, M. *Annu. Rev. Mater. Res.* **2003**, *33*, 129−154.

(8) (a) Yamada, T.; Sadakiyo, M.; Kitagawa, H. *J. Am. Chem. Soc.* **2009**, *131*, 3144−3145. (b) Sadakiyo, M.; Yamada, T.; Kitagawa, H. *J. Am. Chem. Soc.* **2009**, *131*, 9906−9907. (c) Okawa, H.; Shigematsu, A.; Sadakiyo, M.; Miyagawa, T.; Yoneda, K.; Ohba, M.; Kitagawa, H. *J. Am. Chem. Soc.* **2009**, *131*, 13516−13522. (d) Shigematsu, A.; Yamada, T.; Kitagawa, H. *J. Am. Chem. Soc.* **2011**, *133*, 2034−2036. (e) Sahoo, S. C.; Kundu, T.; Banerjee, R. *J. Am. Chem. Soc.* **2011**, *133*, 17950−17958. (f) Colodrero, R. M. P.; Olivera-Pastor, P.; Losilla, E. R.; Aranda, M. A. G.; Leon-Reina, L.; Papadaki, M.; McKinlay, A. C.; Morris, R. E.; Demadis, K. D.; Cabeza, A. *Dalton Trans.* **2012**, *41*, 4045−4051. (g) Colodrero, R. M. P.; Papathanasiou, K. E.; Stavgianoudaki, N.; Olivera-Pastor, P.; Losilla, E. R.; Aranda, M. A. G.; Leon-Reina, L.; Sanz, J.; Sobrados, I.; Choquesillo-Lazarte, D.; Garcia-Ruiz, J. M.; Atienzar, P.; Rey, F.; Demadis, K. D.; Cabeza, A. *Chem. Mater.* **2012**, *24*, 3780−3792.

(9) Ponomareva, V. G.; Kovalenko, K. A.; Chupakhin, A. P.; Dybtsev, D. N.; Shutova, E. S.; Fedin, V. P. *J. Am. Chem. Soc.* **2012**, *134*, 15640−15643.

(10) (a) Bureekaew, S.; Horike, S.; Higuchi, M.; Mizuno, M.; Kawamura, T.; Tanaka, D.; Yanai, N.; Kitagawa, S. *Nat. Mater.* **2009**, *8*, 831−836. (b) Umeyama, D.; Horike, S.; Inukai, M.; Hijikata, Y.; Kitagawa, S. *Angew. Chem., Int. Ed.* **2011**, *50*, 11706−11709. (c) Hurd, J. A.; Vaidhyanathan, R.; Thangadurai, V.; Ratcliffe, C. I.; Moudrakovski, I. L.; Shimizu, G. K. H. *Nat. Chem.* **2009**, *1*, 705−710. (d) Mallick, A.; Kundu, T.; Banerjee, R. *Chem. Commun.* **2012**, 8829−8831.

(11) Alberti, G.; Casciola, M.; Donnadio, A.; Piaggio, P.; Pica, M.; Sisani, M. *Solid State Ionics* **2005**, *176*, 2893−2898.

(12) Costantino, F.; Donnadio, A.; Casciola, M. *Inorg. Chem.* **2012**, *51*, 6992−7000.

(13) (a) Xu, Q.; Zhang, Y.; Yi, J.; Yuan, Y.; Mansur, S. *Microporous Microporous Mater.* **2009**, *119*, 68−74. (b) Wu, H.; Liu, C.; Yang, Y.; Chen, J.; Chang, P. R.; Chen, Y. *Polym. Composite* **2010**, *31*, 1938−1946.

(14) (a) Casciola, M.; Donnadio, A.; Sassi, P. *J. Power Sources* **2013**, *235*, 129−134. (b) Donnadio, A.; Casciola, M.; Di Vona, M. L.; Tamilvanan, M. *J. Power Sources* **2012**, *205*, 145−150.

(15) (a) Werner, P. E.; Eriksson, L.; Westdhal, M. *J. Appl. Crystallogr.* **1985**, *18*, 367−370. (b) Boultif, A.; Louer, D. *J. Appl. Crystallogr.* **2004**, *37*, 724−731.

(16) Laugier, J.; Bochu, B. LMGP-Suite, ENSP/Laboratoire des Materiaux et du Genie Physique, BP 46, 38042 Saint Martin d'Heres, France.

(17) Favre-Nicolin, V.; Cerny, R. *J. Appl. Crystallogr.* **2002**, *35*, 734−743.

(18) Larson, C.; von Dreele, R. B. *Generalized Crystal Structure Analysis System*; Los Alamos National Laboratory: Los Alamos, NM, 2001.

(19) Altomare, A.; Burla, M. C.; Camalli, M.; Cascarano, G. L.; Giacovazzo, C.; Guagliardi, A.; Moliterni, A. G. G.; Polidori, G.; Spagna, R. *J. Appl. Crystallogr.* **1999**, *32*, 115−119.

(20) Sheldrick, G. M. *Acta Crystallogr.* **2008**, *A64*, 112−122.

(21) (a) Pica, M.; Donnadio, A.; Capitani, D.; Vivani, R.; Troni, E.; Casciola, M. *Inorg. Chem.* **2011**, *50*, 11623−11630. (b) Balzar, D.; Audebrand, N.; Daymond, M.; Fitch, A.; Hewat, A.; Langford, J. I.; Le Bail, A.; Louër, D.; Masson, O.; McCowan, C. N.; Popa, N. C.; Stephens, P. W.; Toby, B. H. *J. Appl. Crystallogr.* **2004**, *37*, 911−924.

(22) Guinebretière, R. *X-ray Diffraction by Polycrystalline Materials*; ISTE Ltd: London, 2007.

(23) (a) Thompson, P.; Cox, D. E.; Hastings, J. B. *J. Appl. Crystallogr.* **1987**, *20*, 79−83. (b) Finger, L. W.; Cox, D. E.; Jephcoat, A. P. *J. Appl. Crystallogr.* **1994**, *27*, 892−900.

(24) Toby, B. H. *J. Appl. Crystallogr.* **2001**, *34*, 210−213.